Simultaneous high-speed PIV and PLIF on oxycombustion turbulent flames

Laura Pirateque-Henao[1], Corine Lacour[1], Armelle Cessou[1], David Honoré[1], Bertrand Lecordier[1,*]

1: INSA Rouen Normandie, Univ Rouen Normandie, CNRS, Normandie Univ, CORIA UMR 6614, F-76000 Rouen, France
*Corresponding author: bertrand.lecordier@coria.fr

Keywords: High-speed PIV, High-speed PLIF, Oxyfuel combustion, CCUS.

ABSTRACT

The use of methane oxyflames diluted with CO_2 as a method for carbon capture for utilization and sequestration is a promising method to decarbonize the industrial sector. This article focuses on the study of the flame-aerodynamic interaction of turbulent jet flames obtained with a coaxial burner, particularly on the local extinction zones. This is done thanks to the utilization of simultaneous high-speed (10 kHz) 2D-PIV and OH-PLIF. A temporal and spatial conditional average of the velocity fields is used to observe the common aerodynamic structures linked to a local extinction zone. Additionally, a low-order Proper Orthogonal Decomposition is used to better observe the effects of large turbulent structure on the flame stability. Finally, due to the high range of velocities present on the flow, the calculation of small velocities present on the zone external to the jet are not properly estimated. To improve these measurements, a velocity field integrating two time intervals vector calculations is proposed, allowing the integration of valid velocities on the slow and rapid zones.

1. Introduction

During recent years an important annual increase of the global temperature has been registered (European Enviroment Agency, 2025). A representative contribution to this phenomenon are the green house gases emissions generated by the industrial sector. With the goal to minimize the impacts to the climate, several laws had been implemented to limit these emissions. Furthermore, several national and European strategies have been proposed to reduce completely the emission of greenhouse gases as carbon dioxide (CO_2) such as the Net zero proposed by the European Commission (2023). This can be achieved by different strategies such as switching the fuel to a non-carbon based one, electrification or Carbon Capture for Utilization and Sequestration (CCUS). The last one is of particular interest for the hard-to-abate industry, where the CO_2 emission is inherent to the production process. Moreover, according to the International Energy Agency (2019), the CCUS implementation represents 21% of the efforts to achieve the stated polices scenario stipulated to obtained a net zero CO_2 emissions for 2050.

Carbon Capture for Utilization and Sequestration consists on capturing the CO_2 from the flue gas, before its emission to the atmosphere. Once captured, this gas will be, either, used in other production processes that require it as a raw material (*Projet Take Kair*, 2024), or to be permanently sequestrated into geological underground fields (Wang, 2024). However, the high amount of nitrogen (N_2) present in the flue gas makes CO_2 capture difficult. For this reason oxycombustion (fuel/O_2) can be used to obtain flue gas rich on CO_2 without N_2. However, without the thermal ballast of nitrogen, the combustion temperatures can reach very high values, putting at risk the equipment which, in most industries, are not designed to withstand these temperatures. To reduce the combustion temperatures the oxidizer is commonly diluted with a fraction of the CO_2 captured from the flue gas, this is called a recirculation of flue gas, RFG. Nevertheless, due to different chemical and physical properties of CO_2 and N_2 (Ditaranto & Oppelt, 2011; Chen et al., 2012), this dilution leads to different flame behaviors that requires further study in order to widely implemented oxycombustion as a CCUS method.

Simultaneous Particle Image Velocimetry (PIV)and Planar Laser Induced Fluorescence (PLIF) is widely used for the combined study of flame structure and aerodynamic behaviors. Furthermore, using these laser diagnostics with a high repetition rate gives an unique insight on the extinction processes. For example, Böhm et al. (2009) used 5 kHz PIV/PLIF in turbulent opposed jet flames to observe the time-resolved evolution of vortex-flame interaction, by studying a time sequence of vorticity and strain fields leading to the occurrence of flame extinctions. Similarly, Rajamanickam et al. (2023) used 10 kHz PIV/PLIF on bluff body turbulent flames to observe the local extinction and re-ignition mechanisms on different rates of hydrogen enriched methane flames. In this study, simultaneous 10 kHz PIV/PLIF will be used to observe the flame-aerodynamics interaction present on local extinction events.

Non-premixed jet flames are largely used on industrial furnaces and boilers. To study these flames, a canonical tri-coaxial burner is used. The burner fuel injection is in the center and the oxidizer in the external annular jet. However, due to the burner configuration, the mean injection velocity is 3.3 times higher than the external annular one. This imposes some difficulties on the extraction of information of the velocity fields through classical analyses. This article presents some methods to address this issue, such as conditional averaging, Proper Orthogonal Decomposition (POD) filtering and the integration of two time intervals (dt) on a single velocity field.

2. Experimental Setup

The tri-coaxial burner used in this study is shown in Figure 1(a). The fuel injection is done in the inner tube and the oxidizer in the external annular. To improve flame stabilization, a pilot-like flame is obtained by injecting pure oxygen (O2,i) between the fuel and oxidizer jets, corresponding to the 10% of the total O_2 injected. The amount of CO_2 present in the the oxidizer is represented

by α defined by:

$$\alpha = \frac{Q_{CO_2}}{Q_{CO_2} + Q_{O_2}}, \tag{1}$$

where Q corresponds to the volumetric flow rate.

The burner configuration is defined by a parametric study of gas velocities, Reynolds numbers and velocities ratios for a constant nominal thermal power of 23 kW and an equivalence ratio of 0.95. The selected burner configuration is represented in Fig. 1(a). The fuel injection through the central tube has an inner diameter, $D_1 = 4$ mm. The O2,i is injected in the middle annular jet with an external diameter, $D_{2,e} = 6$ mm. Both tubes have a wall thickness of 500 μm. The outward annular section, with an external diameter, $D_{3,e} = 21.2$ mm, corresponds to the $(O_{2,e} + CO_2)$ blend injection.

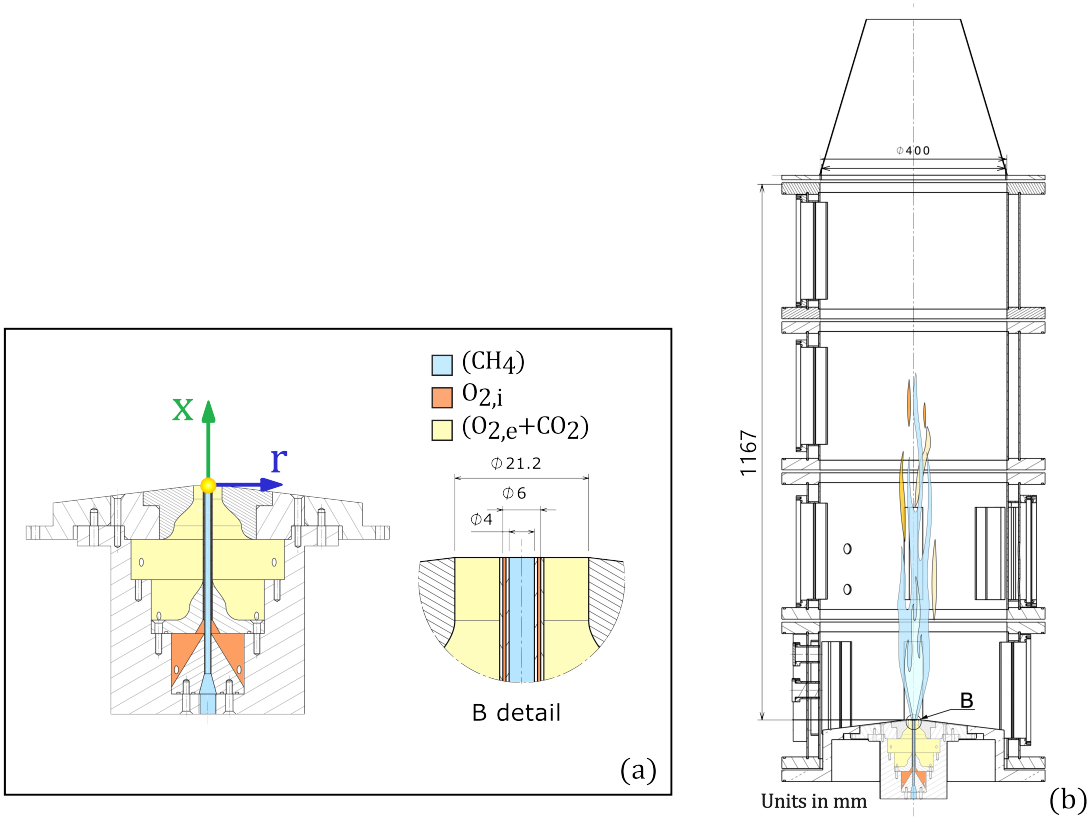


Figure 1. (a) Cross-section of coaxial burner configuration. (b)Cross-section of combustion chamber.

The burner is found in the base of a combustion chamber that prevents the interaction of the flame with ambient air. The chamber, represented in Figure 1(b) has an internal diameter of 400 mm and a height of 1200 mm height. For more or less, all the injection conditions, the mean flame height

is approximately 800 mm, as determined by visual observation. In the lower part of the chamber, quartz windows placed at different angles allow the use of several laser diagnostics and flame imaging techniques.

Characterization of the flame stability limits done in (Pirateque-Henao et al., 2025) shows that for this configuration, the CH_4/O_2 flame presents unstable behavior for a dilution of $\alpha = 65\%$. The study presented in this paper is done under this dilution as well as a reference stable flame at $\alpha = 60\%$. The flow conditions for these to cases are presented on Table 1.

Table 1. Injection parameters

α	$Q_{fuel}\,[m^3(n)/h]$	$Q_{coflow}\,[m^3(n)/h]$	$U_{fuel}\,[m/s]$	$U_{coflow}\,[m/s]$
60%	2.5	12.2	56.1	10.8
65%	2.5	14	56.1	12.4

2.1. High speed OH-PLIF system

The synchronized laser diagnostic setup is shown in Figure 2. The high-speed (10 kHz) OH-PLIF arrangement is represented in purple. The visualization of the reactive zones is done through the excitation of the OH radicals in the Q1(6) line of the $A^2\sum^+ - X^2\prod(1,0)$ transition band, using a Sirah CREDO dye laser emitting at 282.22 nm and $\backsim 1.2$ mJ/pulse. The laser sheet of 46 mm height is obtained with a diverging cylindrical lens and a spherical lens with 1000 mm focal distance to focus the laser sheet at the central axis of the burner.

The acquisition of the fluorescence signal is done with a 1280 x 800 pixel Phantom V2012 camera (spatial resolution of 6.26 pixel/mm), coupled with a fast intensifier, a 105 mm UV lens (CERCO f/2.8) and a band pass filter centered at 310 nm. The field of view for the PLIF images is of 80 x 46 mm^2 and is positioned 2 mm above the burner exit. The acquisition duration is of 4s corresponding to forty thousand frames. The raw images were post-processed by background subtraction, smoothing with a Wiener filter and a correction of the laser sheet inhomogeneties.

2.2. High speed 2D-PIV system

The time-resolved (10 kHz) PIV system, used to investigate the aerodynamic behavior of the flame is represented in Figure 2 in color green. Both PIV and PLIF laser sheets are carefully aligned to ensure perfect overlap of the measurement planes. Additionally, the PLIF laser pulse is temporally synchronized between both PIV pulses. The ZrO_2 particles seeded in each injected flow are illuminated with a Nd:YAG laser at 532 nm and 6 mJ/pulse. The time interval between the two laser pulses is 10 μs. The particle Mie-scattering images are collected with a 1280 x 800 pixel Phantom

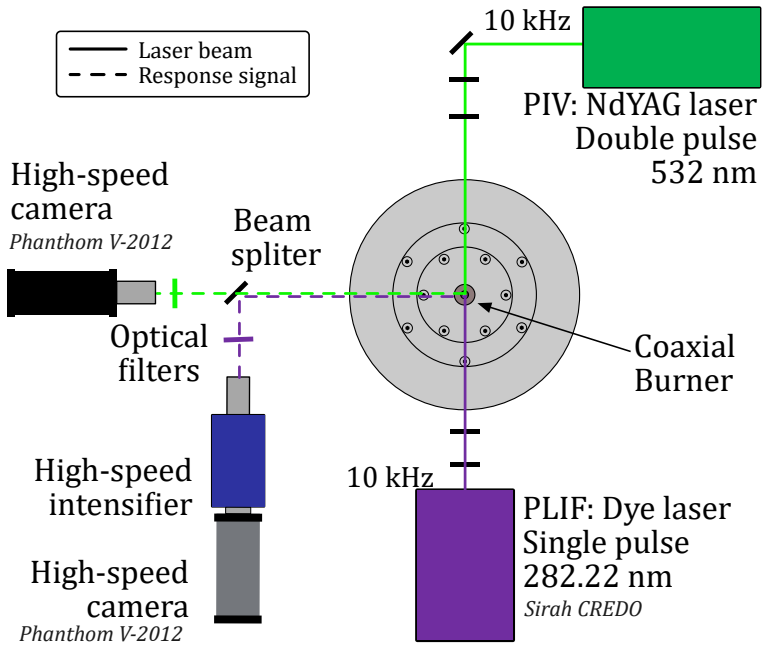


Figure 2. Simultaneous time-resolved (10 kHz) OH-PLIF and PIV set-up

V2012 camera (spatial resolution of 9.55 pixel/mm) equipped with a 180 mm lens (Nikon f/d=2.8) and a 532 nm interference filter to avoid the flame emissions. Similarly to the florescence images, forty thousand double frames were captured. The PIV field of view is of 80 x 133 mm^2. The velocity fields were calculated with a multi-pass adaptive grid and a final calculation window size 24 x 24 pixels (2.5 x 2.5 mm) with an overlap of 75%, resulting in a vector spacing of 0.63 mm. After the combined dewarping of the images, both PIV and PLIF images have a final spatial resolution of 9.55 pixels/mm.

3. Measured fluorescence images and velocity fields

This section presents independently the images obtained by each laser diagnostic. First, the flame structure obtained by high-speed OH-PLIF is shown with some instantaneous binarized fluorescence. This are used to illustrate different types of local extinctions that will be use on the following of the study. Additionally, the mean flame probability is presented to show the general flame structure. The velocity fields obtain by high-speed PIV are then presented using the mean fields in order to illustrate the flow structure obtained with the tri-coaxial burner.

3.1. Flame structure

Figure 3(a) shows instantaneous fluorescence images after binarization for three consecutive flames at $\alpha = 65\%$ separated by 0.2 ms. The flame at instant 0 ms shows a continuous flame exceeding

the laser sheet height in both sides of the flame. The flame at 0.2 ms shows the instant of the flame “break" marked with a red square. At this instant, a local extinction splits the continuous reaction zone into two zones, with the first one attached to the burner. In the flame at instant 0.4 ms, the break, now identified with a yellow square, is convected downstream with the flow. Additionally, a new break can be seen in the left side at a higher location. This study is focus on the origin of the flame breakage, therefore only the first types of breaks are considered, those observed in the instant when the attached flame gets cut. Furthermore, thanks to the flame symmetry, only the results obtained in the left part of the flame will be presented.

In Figure 3(b) the average of the binarized fluorescence images is presented. A higher flame probability is observed near the burner. This is explained by the presence of the pure O_2 injection which creates a pilot-like flame that stabilizes the hole flame.

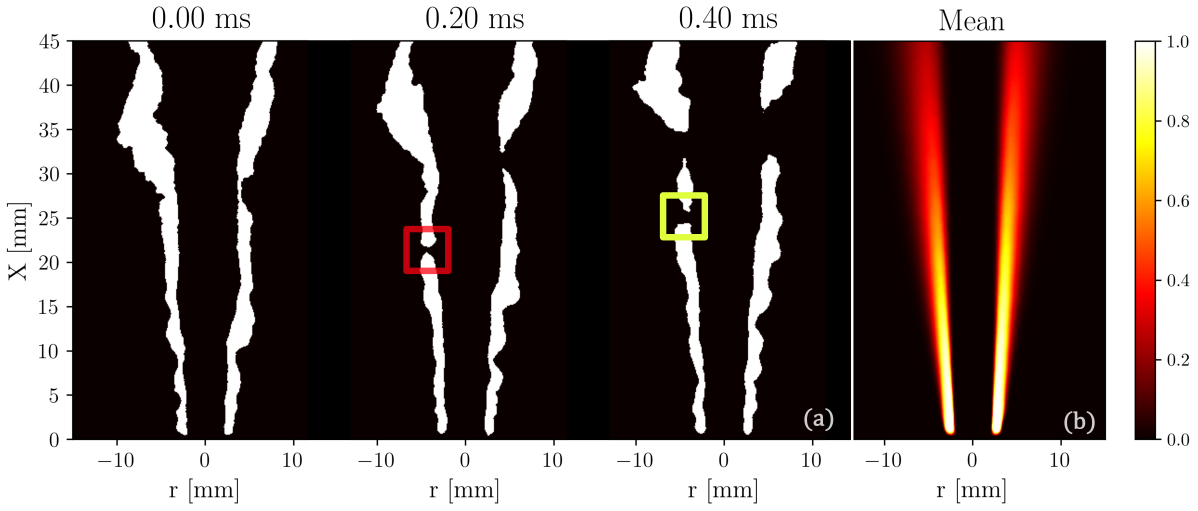


Figure 3. Instantaneous fluorescence images after Otsu binarization and the mean image of the binarized flames at $\alpha = 65\%$. The squares represent flame breaks, red in the moment of flame breakage and yellow for the convected break.

3.2. Tri-coaxial burner mean velocity fields

The mean fields for the case $\alpha = 65\%$ are presented on Figure 4. The mean axial velocity (U), represented in Figure 4(b), shows three zones with different velocities: the central zone is the fuel injection with mean velocities reaching 65 m/s; the second zone is the oxidizer annular injections with velocities between 10 and 20 m/s; and the third zone corresponds to the recirculation of flue gases inside the chamber, where U < 1 m/s. The mean radial velocity (V) is represented in Figure 4(a), where the central and annular jets are diverging from the central axis with absolute velocities between 1 and 3 m/s. Similarly to the axial velocities, the external recirculation has absolute radial velocities inferior to 1 m/s.

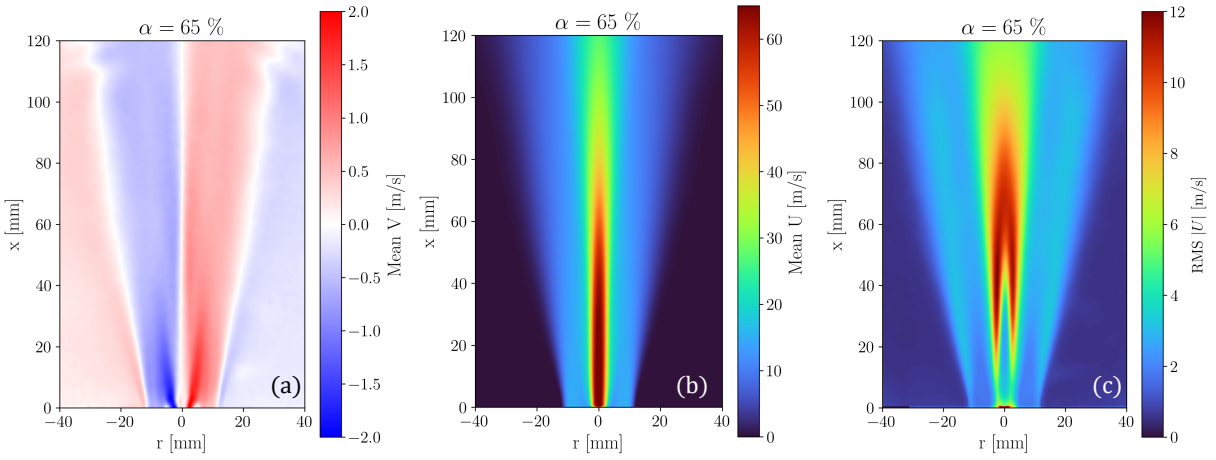


Figure 4. Mean velocity fields. (a) Radial velocity. (b) Axial velocity. (c) Velocity norm RMS.

Figure 4(c) shows the RMS of the norm of the velocity. This field is a classical representation of the standard deviation of a coaxial injection, with the lower RMS values right after the burner corresponding to the potential cores of the central and annular jet, as well as a high RMS value in the mixing layer, as explained by Rehab et al. (1997). However, there are no variations or recognizable patterns that could indicate the presence of flame breaks, nor in the velocity fields. For this reason, a conditional average of the velocity fields is done from the point of reference of the break. This conditional averages are presented in the next section.

4. Vector field filtering and processing

4.1. Flame conditional velocity average

The first method employed to extract information from the simultaneous laser diagnostics is a temporal and spatial conditional average of the velocity fields referenced to the instantaneous flame structure. This method allows the observation of the aerodynamic behavior relative to the flame breakage. For the temporal conditioning, the breaks observed in the moment of separation of the first attached reaction zone are isolated (such as the one identified at the second flame in Figure 3(a)) are used. For the spatial conditioning, a window of size 50 x 18 vectors (37.5 x 11.3 mm) is fixed axially and radially to the coordinates of the cusp of the first attached flame, which is the reference position extracted from the fluorescence images. These instantaneous windows, of axes r* and x*, are averaged for all the moments meeting the temporal condition.

Figure 5 shows the conditional average of the velocity components, as well as some of its gradients, for a stable ($\alpha = 60\%$) and an unstable flame ($\alpha = 65\%$), the black dot represents the fixed coordinates of the attached flame cusp. Excepted the axial velocity presented in the first row, some common patterns related to the flame breaks emerge for both dilution rates. In the U windows, the

conditional averaging is less effective due to its high radial gradient, this leads to a smearing of this component, even with the variation of the r reference coordinate. For the case of the radial velocity V, the flame presence effect is visible on top and bellow the break. The two zones of higher intensity, marked in dark blue, at r* = -6 mm show a higher tendency of the annular jet to go outwards. This evidences that the flame acts as a barrier between the annular and the central jet. Conversely, at the break height (x* = 5 mm), the velocity average is closer to zero, this shows a higher interaction of both jets, the annular jet flows towards the central axis and the central jet flows towards the exterior. This behavior is confirmed by the divergence average, where a positive divergence region passes through the break point showing a flow expansion at this height. Additionally, a negative divergence is observed immediately bellow the break, indicating a compression of the flame tip. In the radial cross derivative windows, dv/dx, a change of sign is observed axially at the break height. This pattern created by the local extinction zone for both dilution cases require further study for the understanding on the flame instabilities formation.

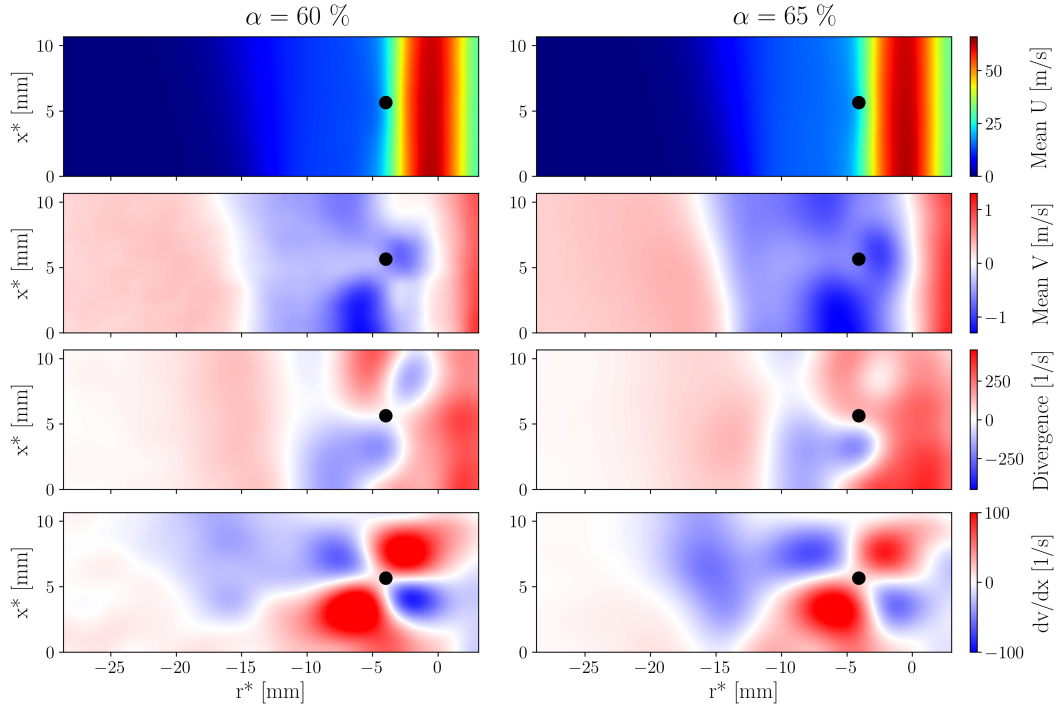


Figure 5. Conditional averaging of the velocity fields and gradients at the moment and in the place of the flame breakage close to the burner. The black dot represents the cusp of the flame where all the windows are fixed for averaging.

4.2. Reduced order POD filtering

As shown in the mean velocity fields in Figure 4, there is an important velocity difference between both coaxial jets, as well as with the external gas recirculation inside the chamber. To better observe the large aerodynamic structures impacting the flame, particularly between the annular jet

and the external recirculation, a low-order POD filtering is employed. This technique has been previously used to discriminate the measured velocities from random error. To identify the number of modes for instantaneous vector fields reconstruction, several criteria can be found in the literature (Raiola et al., 2015; Brindise & Vlachos, 2017; Nekkanti & Schmidt, 2021). For this study, the selected criterion for the cutting mode is the one proposed by Butcher & Spencer (2019), that allows the separation of coherent from stochastic turbulent structures. Full explanation of the method is presented in Butcher & Spencer (2019). The cut-off mode is selected by dividing the acquisition sample in two random sets and then using a cross-correlation of their decomposition modes. Finally, thanks to a correlation threshold the cut-off mode is identified. To employ this method it is necessary that the velocity convergence is ensured for half the sample length. However, according to a convergence test applied to the current sample, this requirement is not met in our configuration. For this reason, the POD modes correlation is made between two series of forty thousand images each. The two series were taken at the same injection conditions but with a difference of few minutes between acquisitions.

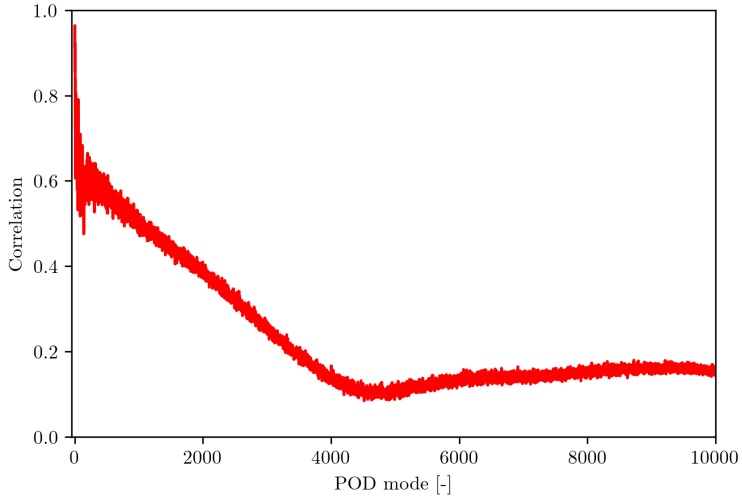


Figure 6. Correlation of POD modes of two acquisition samples at $\alpha = 65\%$.

For each sample the POD with ten thousand modes was calculated with the Python package MODULO (Poletti et al., 2024; Ninni & Mendez, 2020). The correlation between both decomposition is shown in Figure 6. The correlation shows a rapid decay for the first modes and a minimum is reached at 4500 modes, afterwards a slight increase is observed corresponding to the measurement noise. Using the correlation threshold employed by Butcher & Spencer (2019) of 0.6, the coherent structures can be observed until mode 250. Figure 7 shows the superposition of the radial velocity field and the binarized fluorescence images presented in section 3.1 represented by the green region. The top row of the figure shows the measured velocity fields and the bottom row shows the reconstructed velocity field with 250 modes. This filtering is particularly useful in the annular jet zone. In fact, for the presented frames, it allows the identification of large and energetic

structures characteristic of the shear layer between a fast and slow flow. Particularly in this example, at X = 20 mm, a positive structure puts stress on the flame inducing a break in this height. This information was not evident on the original instantaneous images.

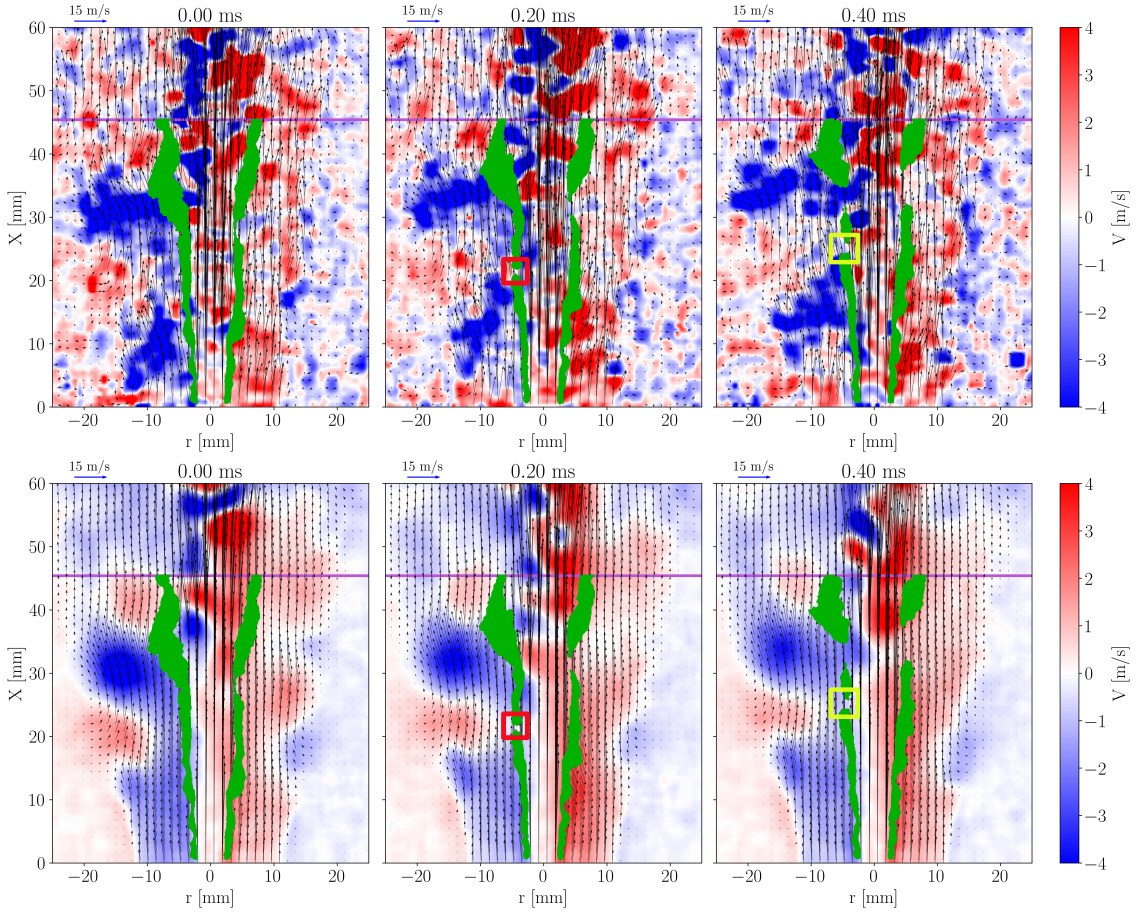


Figure 7. Instantaneous radial velocity fields separated by 0.2 ms, the top row corresponds to the untreated velocity fields and the bottom row to the low order reconstruction with the first 250 POD modes. The green zones represent the binirized fluorescence images presented on Figure 3. The purple line represents the UV laser sheet limit.

The conditional average method used in section 4.1 is now applied to the reconstructed velocity fields. The obtained conditional windows are shown in Figure 8. However, the patterns observed in the measured velocity fields are not longer visible for this amount of modes (second column). A second reconstruction is done using a threshold of modes correlation of 0.4 corresponding to 1800 modes. In this reconstruction the previously observed patterns on the different velocity and gradient conditional averages are once again present. This could indicate that the turbulent structures present in the local extinction zones have a smaller scale. During the following stages of our study, this type of POD filtering will enable us to better understand the topology of the structures involved in the extinction phenomenon.

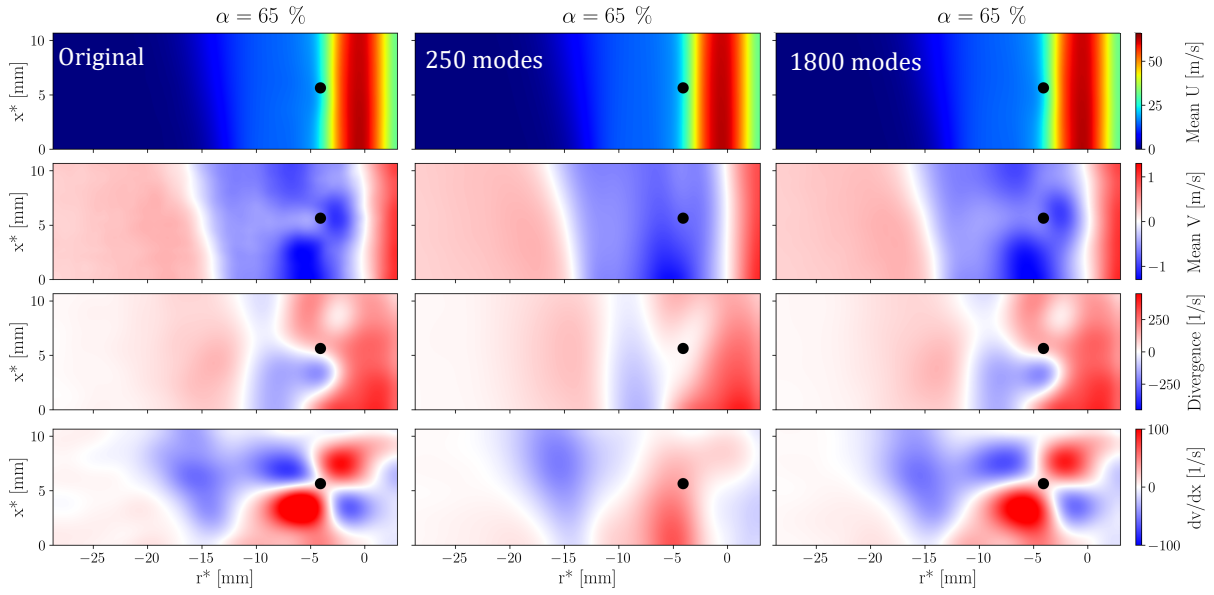


Figure 8. Conditional averaging of the low-order reconstructed velocity fields and gradients on the moment and place of the flame breakage closer to the burner. The black dot represents the cusp of the flame where all the windows are fixed for averaging.

4.3. Multiple time interval PIV calculations

In the previous sections, an analysis has been done concerning the flame instabilities interaction with the coaxial jet. However, it is important to consider that the flame is inside a closed combustion chamber. This confinement leads to a recirculation of hot gases composed by the combustion products. This recirculation, rich on hot CO_2 and water vapor, impacts the flame behavior, however with the current PIV calcualtions it is not possible to correctly observe the flow in this zone. As indicated before, the time interval between the two laser pulses is 10 μs. This dt is selected to obtain particle displacements around 6 px (for a calculation window of 24 x 24 px^2) in the central jet injection and minimize out of motion effects. However, this time interval is not suited for the recirculation zone where particle displacements are lower than 0.1 px and thus have the same level as the measurement noise. Thanks to the time resolved nature of the recordings, a second time interval is available (dt_{tr}), the time between two sets of laser pulses corresponding to 100 μs. This dt_{tr} is now appropriate for the magnitude of the recirculation velocities calculations multiplying the particles displacement by ten. Nevertheless, dt_{tr} it is not suitable to resolve the central jet velocities. In this section a method combining the two intervals of time is proposed to obtain a vector field optimized for small and large velocities.

The velocity calculations for dt_{tr} are done with a pyramidal sum of correlation with 5 levels. The integration of both time intervals is done on each instantaneous velocity fields, by multiplying them with a coefficient matrix that, for each vector, will determine their weight on the final velocity

field:

$$U_{comb} = aU_{Pyr} + bU_{dt}, \tag{2}$$

$$V_{comb} = aV_{Pyr} + bV_{dt}, \tag{3}$$

where the subscripts Pyr and dt represent the velocities calculated with the pyramidal correlation and the standard dt correlation, respectively. And a and b represent the corresponding coefficient matrices. To avoid an abrupt selection of vectors from one calculation method to the other, the following equations are used to determine the coefficient matrices:

$$b = 0.5\left(erf\left(\frac{|U| - th_{vel}}{\sigma}\right) + 1\right), \tag{4}$$

$$a = 1 - b, \tag{5}$$

where the parameter th_{vel} defines the center of the erf function, resulting in $b = 0.5$ meaning that the weight of each calculation method is the same. The σ parameter represents how sharp is the erf function. The value of both coefficients varies between 0 and 1 and are complementary vector-wise to each other. Additionally, special care is taken to avoid the inclusion of masked null vectors (suppressed vectors during the validation stage of the velocity calculation) in the combined field. For this, a condition was included so that if a vector is masked in one of the vector fields, its coefficient is set to zero. In the same way, if a vector is masked in both fields, it will be also masked in the final combined field.

A sensitive analysis was made to select the th_{vel} and σ parameters to determine the best coupling of both calculation methods. This was done by visualization of the instantaneous radial and axial velocity fields. Figure 9 presents three instantaneous fields of the radial velocity, on the top row for the standard dt calculation and in the bottom row for the combined fields. On the standard dt fields, the recirculation zone (-20 mm $< r$ and $r > 20$ mm) is composed by many small velocity variations with different directions. This does not represent the actual slow flow of this zone, but rather the measurement noise. Conversely, in the fields with the combined dt, the recirculation zone is mainly constant and mostly directed towards the central axis, corresponding to the expected flow behavior in this zone. Additionally, the mixing layer between this zone and the annular jet is better defined. Furthermore, the high velocities present in the coaxial jet are conserved.

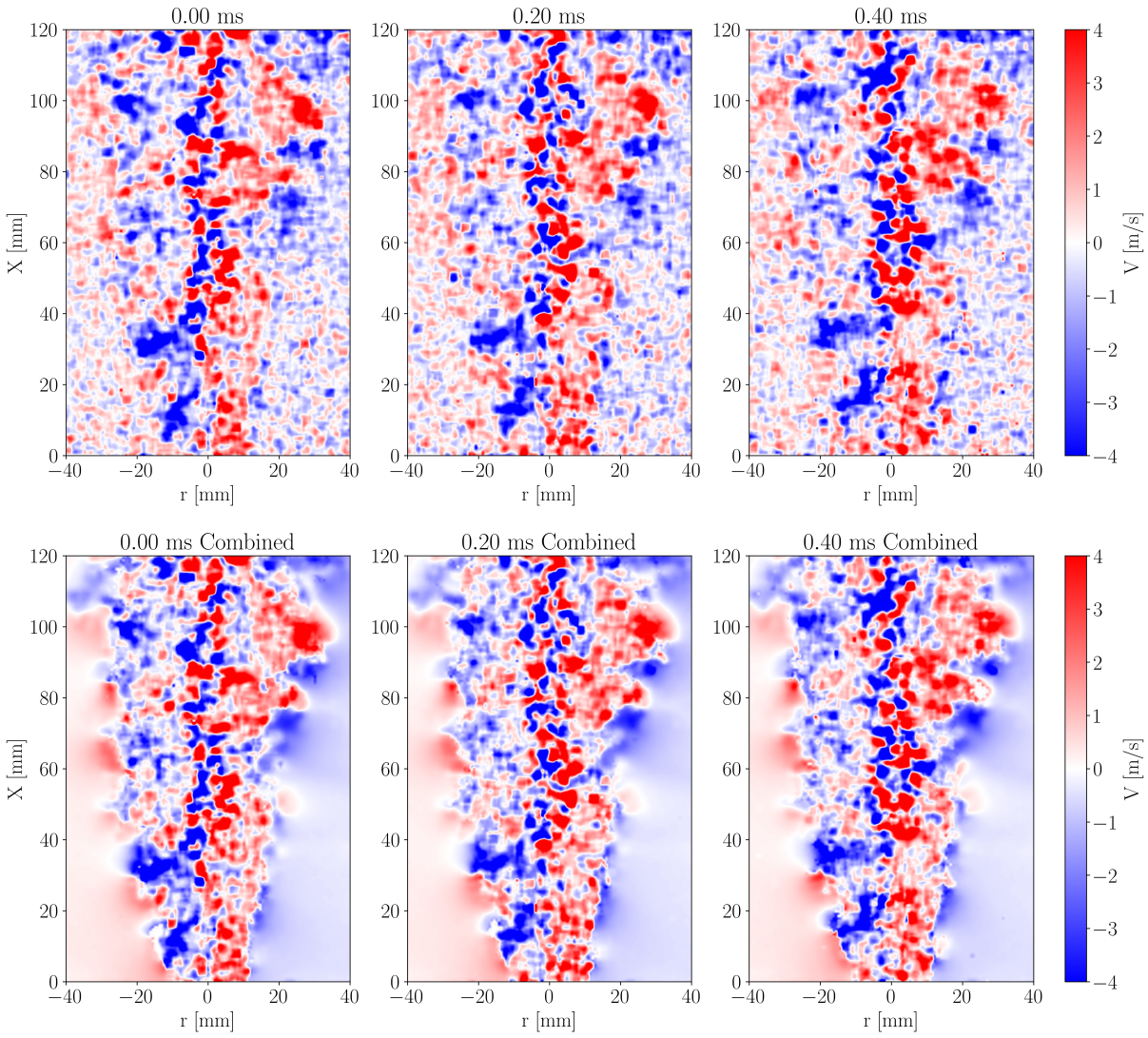


Figure 9. Radial velocity for three instantaneous velocity fields for $\alpha = 65\%$. The top row corresponds to the standard dt calculation and the bottom row to the fields with two dt combination.

In Figure 10, the mean velocity fields are presented. Compared to the average fields presented on Figure 4, the dt combination method did not seem to have an impact in the global flow structure or the global radial and axial velocities. However, the improvement allowed by the additional dt_{tr} velocity calculation is noticeable in Figure 10(a) where the external zone, first, has a smother appearance, and second, the velocity is slightly higher, showing a velocity underestimation with the standard calculation. On the axial field there is also an improvement on the velocities of the external zone, however, on Figure 10(b) it is not evident. This is due to the color scale, which is selected to match the previous mean velocity fields. Nonetheless, the improvement on the velocity norm can be seen in the reduction on its RMS values presented on Figure 10(c), as well as the sharper transition between the recirculation and the annular jet.

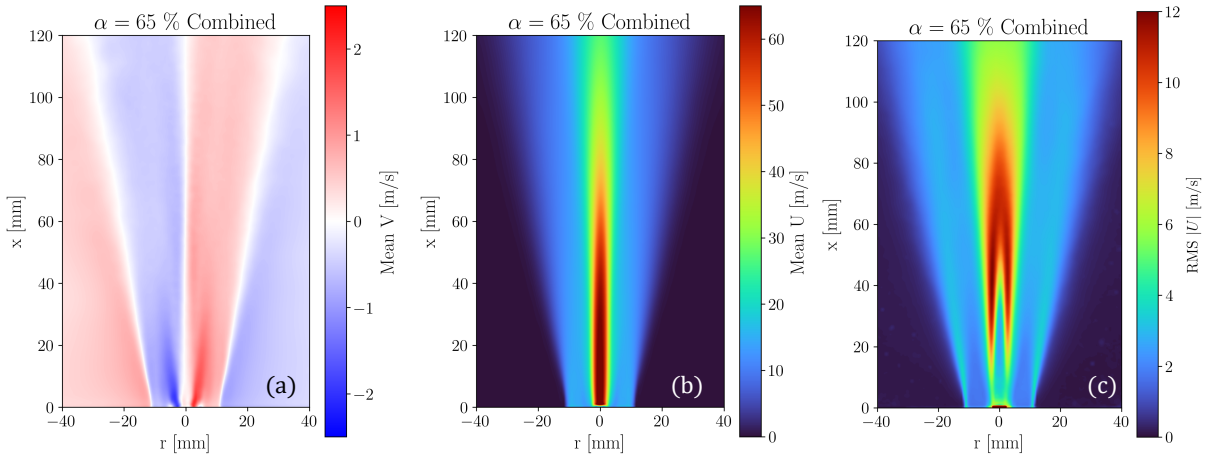


Figure 10. Mean velocity fields with double dt velocity calculation for $\alpha = 65\%$. (a) Radial velocity. (b) Axial velocity. (c) Velocity norm RMS.

The proposed combination method with integration of two time intervals calculations has shown to improve the quality on the final velocity field, particularly on the lower velocities. This allows the study on the effects of the recirculation atmosphere on the high velocity jet flame, which is not possible with the standard single dt calculation or even with the POD filtering. However, for large acquisition samples, as the one used in this study, the independent calculation of the vector fields requires a high amount of time, particularly for the pyramidal correlation. For this reason, we are currently developing a PIV algorithm that integrates both time intervals directly on the velocity calculations, resulting on the integrated velocity field (Lacour & Lecordier, 2025).

5. Conclusions and perspectives

The prevention of climate change requires the implementation of strategies to reduce CO_2 production. Oxycombustion diluted by CO_2 is a promising method for CCUS, to contribute to the industry decarbonation, however it is necessary to better understand the behavior of this flames in a burner that is representative of the industrial requirements.

In this study simultaneous high speed PIV and OH-PLIF was used to observe the interaction of the flame breakage and the aerodynamic field. However, some difficulties to extract information of the velocity fields through classic analysis are encountered due to the flow nature. For this reason, several methods were used to better observe the cross effects of the flame and the coaxial jets. The first method is the temporal and spatial conditional averaging, this allows the observation of the aerodynamic structures with a fixed reference from the flame first break, showing the impact of the presence and absence of a reaction zone on the tri-coaxial jet behavior. The second method is a low-order POD filtering, used to discriminate the large coherent structures from the random structures. This method allowed to highlight the presence of large structures that influence the flame stability.

Additionally, the combination of the first two methods, allowed to understand the nature of the turbulent structures present on the local extinction zones. The third method presented in this work is the integration of two time intervals, one suited for the large velocities of the central jet and the other one suited for the low velocities present in the external jet. This method presented an significant improvement on the external zones, while preserving valid velocities on the central jet.

The application of this three methods will allow the in-depth study of flame-aerodynamics interaction on turbulent jets, to better understand the extinction mechanisms generated by CO_2 in methane oxyflames. Additionally, the improved velocity fields are useful for the validation of numerical simulations on these flames.

Acknowledgements

This work was supported by a French government grant managed by the Agence Nationale de la Recherche under the OXY3C project of the France 2030-PEPR SPLEEN program, reference ANR-22-PESP-0009.

Nomenclature

α	CO_2 dilution of the oxidizer [-]
X	Axial axis coordinates [mm]
r	Radial axis coordinates [mm]
Q	Volumetric flow rate $[m^3(n)/h]$
D	Diameter [mm]
U	Axial velocity [m/s]
V	Radial velocity [m/s]

References

Brindise, M. C., & Vlachos, P. P. (2017). Proper orthogonal decomposition truncation method for data denoising and order reduction. *Experiments in Fluids*, *58*(4), 28. doi: 10.1007/s00348-017-2320-3

Butcher, D., & Spencer, A. (2019). Cross-correlation of POD spatial modes for the separation of stochastic turbulence and coherent structures. *Fluids*, *4*(3).

Böhm, B., Heeger, C., Boxx, I., Meier, W., & Dreizler, A. (2009). Time-resolved conditional flow field statistics in extinguishing turbulent opposed jet flames using simultaneous highspeed PIV/OH-PLIF. *Proceedings of the Combustion Institute*, *32*(2), 1647-1654. doi: https://doi.org/10.1016/j.proci.2008.06.136

Chen, L., Yong, S. Z., & Ghoniem, A. F. (2012). Oxy-fuel combustion of pulverized coal: Characterization, fundamentals, stabilization and CFD modeling. , *38*(2), 156–214. doi: 10.1016/j.pecs.2011.09.003

Ditaranto, M., & Oppelt, T. (2011). Radiative heat flux characteristics of methane flames in oxy-fuel atmospheres. , *35*(7), 1343–1350. doi: 10.1016/j.expthermflusci.2011.05.002

European Commission. (2023). *Proposal for a regulation of the European Parliament and of the Council on establishing a framework of measures for strengthening Europe's net-zero technology products manufacturing ecosystem (Net Zero Industry Act)- Proposal report.*

European Enviroment Agency. (2025). *Global and european temperatures.* Retrieved 28/05/2026, from `https://www.eea.europa.eu/en/analysis/indicators/global-and-european-temperatures`

International Energy Agency. (2019). *World energy outlook 2019.* Retrieved 2025-05-28, from `https://www.iea.org/reports/world-energy-outlook-2019`

Lacour, C., & Lecordier, B. (2025). A new sub-pixel approach based on multi-correlation maps for velocity vector evaluation in PIV algorithms. In *16th International Symposium on Particle Image Velocimetry (ISPIV2025).* Retrieved from `https://hal.science/hal-05144943`

Nekkanti, A., & Schmidt, O. T. (2021). Frequency–time analysis, low-rank reconstruction and denoising of turbulent flows using SPOD. *Journal of Fluid Mechanics*, *926*, A26. doi: 10.1017/jfm.2021.681

Ninni, D., & Mendez, M. A. (2020). MODULO: A software for multiscale Proper Orthogonal Decomposition of data. *SoftwareX*, *12*, 100622. doi: https://doi.org/10.1016/j.softx.2020.100622

Pirateque-Henao, L., Lecordier, B., Lacour, C., Cessou, A., & Honoré, D. (2025). *Experimental study of CO_2 diluted oxycombustion for a decarbonized industry*. European Combustion Meeting. Retrieved from `https://hal.science/hal-05070729`

Poletti, R., Schena, L., Ninni, D., & Mendez, M. A. (2024). MODULO: A Python toolbox for data-driven modal decomposition. *Journal of Open Source Software*, *9*(102), 6753. doi: 10.21105/joss.06753

Projet Take Kair. (2024). Retrieved 2024-11-09, from `https://www.takekair-concertation.fr/blog/2792/les-documents-de-la-concertation-prealable`

Raiola, M., Discetti, S., & Ianiro, A. (2015). On PIV random error minimization with optimal POD-based low-order reconstruction. *Experiments in Fluids*, *56*(4), 75. doi: 10.1007/s00348-015-1940-8

Rajamanickam, K., Lefebvre, F., Gobin, C., Godard, G., Lacour, C., Lecordier, B., … Honoré, D. (2023). Effect of H_2 addition on the local extinction, flame structure, and flow field hydrodynamics in non-premixed bluff body stabilized flames. *Physics of Fluids*, *35*(4), 047110. doi: 10.1063/5.0142921

Rehab, H., Villermaux, E., & Hopfinger, E. J. (1997). Flow regimes of large-velocity-ratio coaxial jets. , *345*, 357–381. doi: 10.1017/S002211209700637X

Wang, R. (2024). Status and perspectives on CCUS clusters and hubs. *Unconventional Resources*, *4*, 100065. doi: https://doi.org/10.1016/j.uncres.2023.100065